IEEE Access
Multidisciplinary ⋮ Rapid Review ⋮ Open Access Journal

Received 11 December 2024, accepted 23 December 2024, date of publication 30 December 2024, date of current version 3 January 2025.

Digital Object Identifier 10.1109/ACCESS.2024.3523596

RESEARCH ARTICLE

Industrial Monitoring of Residue Deposition in Semiconductor Process Exhaust Pipelines Using Electrical Capacitance Measurements

MINHO JEON[1], ANIL KUMAR KHAMBAMPATI[1], JONG HYUN SONG[2], KEUN JOONG YOON[3], AND KYUNG YOUN KIM[1,4]

[1]Department of Electronics engineering, Jeju National University, Jeju 63243, South Korea
[2]Nano Process Technology Department, KAIST Affiliated National Nano Fab Center, Daejeon 34141, South Korea
[3]Prosen Company Ltd., Incheon 21984, South Korea
[4]Kyoto College of Graduate Studies for informatics, Kyoto 606-8225, Japan

Corresponding author: Kyung Youn Kim (e-mail: kyungyk@jejunu.ac.kr; k_kim@kcg.edu)

This work was supported in part by the Semiconductor Business Innovation Development Project of National Nano Fab Center (NNFC) in 2023, and in part by the Basic Science Research Program through the National Research Foundation of Korea (NRF) funded by the Ministry of Education under Grant 2022R1I1A3053600.

ABSTRACT In semiconductor manufacturing, the accumulation of byproducts in exhaust pipelines under inadequate temperature control poses significant safety and operational risks. This study introduces an innovative approach employing an electrical capacitance measurement sensor system combined with an artificial neural network (ANN) to monitor residue buildup. The proposed method estimates the free volume index within industrial process exhaust pipes, enabling precise evaluation of residue deposition and gas phase fractions. Numerical simulations and field studies in semiconductor environments validate the model's effectiveness, demonstrating accurate residue quantification and enhancing safety and operational efficiency. In numerical simulations, the error between true values and estimated values was within 1%, while the values estimated from experimental data showed an error within 5%. These findings underscore the robustness of the model in both controlled and real-world settings. This advancement offers a practical and reliable solution to mitigate hazards and optimize maintenance processes in semiconductor manufacturing.

INDEX TERMS Electrical capacitance measurement, semiconductor process, pipe deposition monitoring, free volume index, artificial neural network (ANN).

NOMENCLATURE

ANN	Artificial neural network.
PM	Periodic maintenance.
CMD	Computational fluid dynamics.
MSE	Mean squared error.
Tanh	Hyperbolic tangent.
SGD	Stochastic gradient descent.
RMSprop	Root mean squared propagation.
EMA	Exponential moving average.
MSPE	Mean square percentage error.
MAE	Mean absolute error.
RMSE	Root mean square error.
CVD	Chemical vapor deposition.
ECT	Electrical capacitance tomography.
WO_3	Tungstite.
TiO_2	Titanium dioxide.
Al_2O_3	Aluminium oxide.
$\boldsymbol{\varepsilon}(\boldsymbol{x},\boldsymbol{y})$	Permittivity distribution within sensing region.
$\boldsymbol{\phi}(\boldsymbol{x},\boldsymbol{y})$	Electrical potential distribution.
$\boldsymbol{C}$	Capacitance.
$\boldsymbol{\Delta V}$	Difference voltage.
$\boldsymbol{\Gamma}$	Electrode surface.
$\boldsymbol{\lambda}$	Normalized capacitance vector.
$\boldsymbol{S}$	Sensitivity matrix.
$\boldsymbol{x}$	Normalized permittivity vector.
$\boldsymbol{\alpha}$	Free volume index.
r	Inner radius.
d	Thickness.
A_{pipe}	Area of the industrial process pipe.

The associate editor coordinating the review of this manuscript and approving it for publication was Jolanta Mizera-Pietraszko.

A_{gas}	Empty area of pipe.
$A_{deposit}$	Residue deposit region.
$\boldsymbol{W}$	Weight matrix.
$\boldsymbol{b}$	Bias.
$\boldsymbol{\varphi}$	Activation function.
$\boldsymbol{Y}$	Output of ANN.
$\boldsymbol{\gamma}$	Loss value.
$\boldsymbol{Y_i}$	Estimated output.
$\boldsymbol{Y_{true}}$	True output.
$\boldsymbol{\eta}$	Learning rate.
$\boldsymbol{w_t}$	Weight coefficient in each neuron in epoch $\boldsymbol{t}$.
$\boldsymbol{L}$	Loss function.
$\frac{\partial L}{\partial W_t}$	Gradient matrix.
$\boldsymbol{\tau}$	Update coefficient of exponential moving average.
$\boldsymbol{g_t}$	Gradient cumulative size up.
$\hat{m}^t$	First momentum.
$\hat{v}^t$	Second momentum.
$\boldsymbol{\beta_1}$ and $\boldsymbol{\beta_2}$	Momentum decay rate.
α_i^{true}	True free volume indexes.
α_i^{est}	Estimated free volume indexes.
α^{est}	Mean of all estimated free volume index values.

I. INTRODUCTION

Byproducts from semiconductor metal processing facilities contain WO_3, TiO_2, and Al_2O_3 substances [1], [2], [3]. Due to their strong toxicity and corrosiveness, these byproducts harm the atmospheric environment, either alone or in combination [4]. Additionally, in the case of scrubbers used by semiconductor manufacturers, the dust and residues from harmful gases transform into resin form during decomposition in the scrubber and firmly adhere to the inner walls of the pipes. Continuous heat exposure causes these toxic gases to harden into powder form, which can create high-risk situations by blocking the interior of the pipe [2], [3]. To reduce pipe clogging, water is artificially sprayed sometimes at the scrubber's exhaust end to remove the residues from the inner walls. However, this process requires caution, as increased moisture flow into the secondary scrubber can reduce its performance [2]. Failure to promptly treat the residual buildup generated during the semiconductor process can block waste gas flow, disrupt the completion of the process, and pose a high risk of explosion. Therefore, periodic maintenance (PM) is essential, where personnel manually dismantle and clean the scrubber equipment or inlet pipes [5]. In particular, primary scrubbers with smaller processing capacities have shorter PM cycles and require careful management. Currently, PM workers visually inspect residual buildup, potentially exposing themselves to harmful environments. To safeguard PM workers' health and safety, it is necessary to implement regular, non-destructive monitoring of the pipeline at the rear end of the process.

The percentage of the phase fractions in a pipe can be assessed through various methods, such as, radiation attenuation (using X-rays or γ-rays) [6], [7], [8], probes involving optical or electrical contact [9], electrical impedance based or capacitive based sensing [10], and using quick-closing valves [11]. While probe-based methods disrupt the flow field, radiation attenuation methods are both costly and present challenges, particularly regarding radiation safety. Conversely, impedance-based techniques are practical and cost-effective [11], [12]. The primary benefit of applying capacitive sensing methods is their non-intrusive nature, which ensures minimum disruption of fluid flow. Electrical capacitance measurement techniques are used for real-time monitoring in diverse industries [13], [14]. These techniques are instrumental in monitoring multiphase flows in oil and gas pipelines [15], measuring void-fraction by capacitance sensor [13], optimizing pharmaceutical and food processes [16], and improving mineral processing efficiency [17]. Additionally, ECT has applications also include biomedical imaging for non-invasive lung visualization [18] and environmental monitoring [19], [20].

The semiconductor process exhaust pipeline involves the flow of residue gas byproducts, which includes a solid-gas flow visualization. Monitoring techniques based on electrical capacitance measurement can observe and monitor the distribution and behavior of solid particles within a gas phase in real time. By analyzing the variations in capacitance measured at the electrodes, insights can be gained into the dielectric constant distribution within the pipe, as well as the concentration and movement of materials [21], [22]. The pipe, comprising distinct phases with varied compositions, contributes to different electrical properties, leading to distinct permittivity distributions. Void fraction is crucial for understanding the flow characteristics and behavior of multiphase flow systems [23], [24], [25], [26], [27]. It is often expressed as a percentage ranging from 0% (no voids, solid-packed) to 100% (completely open, with no solid particles). Traditional methods for void fraction estimation such as image reconstruction and computational fluid dynamics (CFD), often rely on complex physical models and extensive experimental data, which can be time-consuming, expensive, and subject to inherent limitations [23], [28], [29]. Additionally, in a gas scrubber system, where high-temperature thermochemical reaction occurs [2], the permittivity of materials inside the pipe is also changed. Each chemical has a unique relationship between temperature and permittivity value [30], [31], so this must be considered when measuring capacitance. Capacitance-based sensing has emerged as a crucial technology for void fraction measurement in two-phase flows, with significant advancements made in recent years. An asymmetric capacitance sensor with FEM-based calibration was developed to address non-linear capacitance relationships, achieving high accuracy but limited to specific refrigerants and flow conditions [32]. To enhance sensor sensitivity, a ''skewed'' design

with notable performance improvements is proposed [33], and sensor configurations for gas-liquid flows is optimized, addressing issues of sensitivity and linearity [34]. However, both studies highlighted the need for further validation in real-world applications.

In contrast, artificial neural networks (ANN) offer a data-driven approach to void-fraction estimation, leveraging their ability to learn intricate patterns and relationships from large datasets [23], [28], [29]. By training ANNs on a diverse range of input features and corresponding void-fraction measurements, these networks can provide robust and accurate predictions, even in cases where traditional methods may fall short. An ANN-based model was applied to annular two-phase air-water flow in [23] to estimate the liquid phase void fraction. The above approach considers a simple two-electrode sensor with static annular flow conditions. However, the semiconductor process involves solid-gas flow in metal pipes that require multiple electrode geometries, and the flow conditions are not always annular. The developed ANN model must estimate the free volume index of gas in complex eccentric flow conditions, which are typically observed in semiconductor processes involving exhaust residue deposits.

Capacitance sensors with artificial neural networks (ANNs) was integrated for annular flows, showing excellent prediction accuracy in simulations but lacking industrial validation [35]. Similarly, MLP (multilayer perceptron)-based systems were explored, achieving high accuracy in homogeneous flows. but facing challenges in applying these methods to complex industrial environments [33], [36].

Building on these foundations, this study integrates an electrical capacitance measurement system with an ANN to enable real-time monitoring of residue buildup in exhaust pipelines, bridging the gap between simulation-based research and practical industrial application. This approach aims to enhance safety and operational efficiency in semiconductor manufacturing by addressing the limitations of prior works.

In this study, an Artificial Neural Network (ANN) approach optimized with a grid search method is proposed to estimate the free volume index, enabling effective monitoring of exhaust residue deposits in semiconductor process pipelines within an industrial setting. The ANN model is trained with capacitance data generated from various random permittivity distributions of gas and residue deposits inside the pipe as input while the corresponding free volume index serves as the output.

The main contributions of the present work lie in the following

1. The idea of utilizing ANNs with grid search technique for estimating free volume index directly in solid-gas flow using electrical capacitance measurements without image reconstruction
2. Train the model for estimating free volume index not only involving simple annular flow but complex flow patterns involving eccentric and random situations in semiconductor process exhaust pipeline
3. Different activation functions and optimization methods are used with ANNs for free volume index and the performance is compared
4. Detailed numerical studies and industrial field studies at the semiconductor process plant are carried out to demonstrate the effectiveness of the proposed free volume index estimation

II. METHOD

A. ELECTRICAL CAPACITANCE MEASUREMENT

Semiconductor metal processing facilities generate residue gases transported through metal pipes under very high-pressure conditions. Therefore, the electrical capacitance measurement sensor modelled for such applications has electrodes in contact with the medium. In pipe deposition monitoring using the sensor, we measure the change of capacitance based on the permittivity distribution corresponding to the material distribution inside an industrial pipe or vessel of interest (Fig. 1). This is done by measuring the capacitances between all electrode pairs that are placed around the periphery of the pipe.

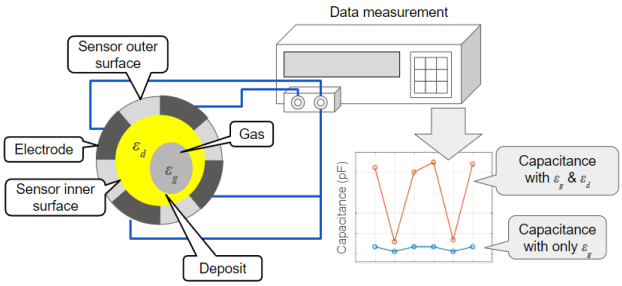

FIGURE 1. Pipe residue deposition monitoring using electrical capacitance tomography.

The relationship between measured electrical capacitance value and permittivity distribution of gas and residue deposit inside a pipe is obtained from forward problem of electrical capacitance tomography. Considering that the total electric flux over the electrode's surface is zero, the permittivity distribution and potential are related through Maxwell's equation as [12]

$$\nabla\cdot[\varepsilon(x,y)\nabla\phi(x,y)] = 0 \tag{1}$$

where $\varepsilon(x,y)$ is the permittivity distribution within sensing region, $\phi(x,y)$ is the electrical potential distribution. For inhomogeneous permittivity distribution, the capacitance C can be computed using FEM (finite element method) numerically as,

$$C = \frac{1}{\Delta V}\oint_{\Gamma}\varepsilon(x,y)\nabla\phi(x,y)d\Gamma \tag{2}$$

where ΔV is the difference voltage measured between the source and detector and Γ is the electrode surface. From the above equation, we calculate the capacitance based on

the permittivity distribution of gas and residue deposit inside pipes inner wall at each given scenario. In general, the measured capacitance between the electrode combinations and the permittivity distribution $\varepsilon(x, y)$ are nonlinearly related, such as

$$C = f(\varepsilon) \tag{3}$$

The above Eq. (3) can be expressed as a linear approximation [12], [37], i.e.

$$\lambda = Sx \tag{4}$$

where λ is the normalized capacitance vector, S is sensitivity matrix, and x is the normalized permittivity vector. For more details about ECT forward problem see [12]

B. FREE VOLUME INDEX CALCULATION OF PIPE

Let us consider the inner radius r of the pipe and the thickness d of the residue deposit as shown in Fig. 2. The area of the industrial process pipe is $A_{pipe} = \pi r^2$, and the empty area of pipe where the exhaust residue gas flows is $A_{gas} = \pi(r-d)^2$. The residue deposit region is $A_{deposit} = \pi r^2 - \pi(r-d)^2$. Therefore, the free volume index α is calculated as follows

$$Free\ volume\ index\ (\alpha) = \frac{A_{gas}}{A_{pipe}} = \frac{\pi\,(r-d)^2}{\pi r^2} = \frac{(r-d)^2}{r^2} \tag{5}$$

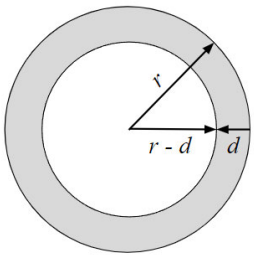

FIGURE 2. Illustration of void fraction computation in pipe deposition monitoring.

III. ANN MODEL FOR RESIDUE DEPOSITION MONITORING

A. AN OVERVIEW OF AN ARTIFICIAL NEURAL NETWORK MODEL

Artificial Neural Networks (ANNs) are particularly useful for estimating void fraction because they can capture the complex, non-linear correlations between capacitance measurements and the internal phase configuration. By training ANNs with capacitance data, the model learns to identify patterns and associations between the input data (capacitance readings) and the corresponding output (free volume index or permittivity distribution), enabling more accurate predictions even in challenging, fluctuating environments, positioning ANNs as a valuable tool for monitoring and optimizing industrial processes.

The process for estimating free volume index using an Artificial Neural Network (ANN) involves several critical stages. Initially, capacitance measurement data, which captures the phase distribution within a pipeline, is gathered and undergoes preprocessing, including normalization. This dataset is then divided into training, validation, and test subsets. The ANN architecture is then designed, typically with input, hidden, and output layers; the input layer corresponds to the capacitance data, while the output layer is responsible for predicting the void fraction. During training, forward propagation is employed to generate predictions, and backpropagation is used to adjust network weights by minimizing the error, often based on a loss function such as Mean Squared Error (MSE), and by applying optimization techniques to enhance learning efficiency. Throughout training, performance is validated to prevent overfitting, and hyperparameters are fine-tuned for improved results. Once the training phase concludes, the network is evaluated using the test set to assess its ability to generalize. Finally, the performance of the ANN is assessed using performance metrics ensuring accurate and reliable void fraction estimation in practical industrial applications.

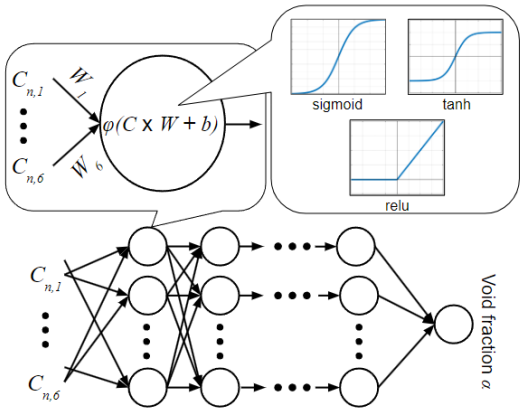

FIGURE 3. Structure of the proposed neural network model and activation function for void fraction monitoring inside a pipe.

B. FORWARD PROPAGATION OF THE ANN MODEL

Fig. 3 shows the forward propagation of artificial neural network model for free volume index estimation. In the forward propagation of the ANN, the following equation is utilized for free volume index estimation [38], [39],

$$Y = \varphi(C*W + b) \tag{6}$$

where C is the capacitance vector, W is the weight matrix, and b is a bias. The function φ is the activation function, which gives a non-linear nature to the output$Y$. We have used sigmoid, *tanh* (hyperbolic tangent) and *Relu* as three activation functions in the tuning process, and the equations are as follows [40],

$$Relu(x) = x(x \geq 0), Relu(x) = 0(x < 0) \tag{7}$$

$$tanh(x) = \frac{e^x - e^{-x}}{e^x + e^{-x}} \tag{8}$$

$$Sigmoid(x) = \frac{1}{1 + e^{-x}} \tag{9}$$

The capacitance value is provided to the hidden layer through the input layer. In each hidden layer neuron, the provided capacitance value applies the activation function from the previous equation. As network's last layer, the output layer shows estimation results for free volume index.

C. BACKPROPAGATION OF THE ANN MODEL

In backpropagation, the weight coefficient of each neuron is updated to reduce the loss value, which is calculated with true output and estimated output Y through forward propagation. The loss value is defined as follows [41],

$$\gamma = \frac{1}{n}\sum_{i=1}^{n}(Y_i - Y_{true})^2 \tag{10}$$

where γ is the loss value, Y_i is estimated output in forward propagation, Y_{true} is true output that corresponds to input capacitance C, and the number of data n. This paper uses three optimization methods, SGD (stochastic gradient descent), RMSprop (Root mean squared propagation) and Adam (adaptive moment estimation), to update weights in the network grid. SGD optimization equation is defined as [42],

$$w_{t+1} = w_t - \eta\frac{\partial L}{\partial W_t} \tag{11}$$

where η is the learning rate, w_t is the weight coefficient in each neuron in epoch t, L is the loss function defined in mini-batch, $\frac{\partial L}{\partial W_t}$ is a gradient matrix computed with respect to the weight coefficient. SGD has a low computational cost and fast convergence as two presentative advantages but is noise-sensitive. RMSprop optimizer adjusts the learning rate for each variable at every epoch. Rather than simply accumulating the slope from the previous time step at the same rate, the slope is updated using an exponential moving average (EMA). Equation is defined as follows [42],

$$g_t = \gamma g_{t-1} + (1-\gamma)(\nabla f(w_{t-1}))^2 \tag{12}$$

$$w_{t+1} = w_t - \frac{\mu}{\sqrt{g^t + \theta}}\nabla f(w_{t-1}) \tag{13}$$

where g_t is the gradient cumulative size up to the tth time step, γ is update coefficient of exponential moving average, θ is set to 10^{-8} to prevent denominator from being 0. Adam optimization combines the method of two ideas, momentum and RMSprop, and is defined as follows [42],

$$w_{t+1} = w_t - \mu\frac{\hat{m}^t}{\sqrt{\hat{v}^t + \theta}} \tag{14}$$

$$\hat{m}^t = \frac{m^t}{1-(\beta_1)^t} \tag{15}$$

$$\hat{v}^t = \frac{v^t}{1-(\beta_2)^t} \tag{16}$$

$$m^t = \beta_1 m^{t-1} - (1-\beta_1)\nabla_w \gamma^t(w^{t-1}) \tag{17}$$

$$v^t = \beta_2 v^{t-1} - (1-\beta_2)\left\{\nabla_w \gamma^t(w^{t-1})\right\}^2 \tag{18}$$

where the default value for θ is set to 10^{-8} and μ is the step size at 10^{-5} for updating the first momentum $\hat{m}^t$ and second momentum $\hat{v}^t$. β_1 and β_2 are each momentum decay rate and set to 0.9 and 0.999, respectively. In the calculation, all operations on vectors are element-wise.

D. HYPERPARAMETER SELECTION BY GRID SEARCH TECHNIQUE AND TRAINING PROCESS

In order to identify the optimal configuration, we employ the grid search technique, which involves exploring different combinations of hyperparameters such as the number of hidden layers, neuron quantity per layer, activation functions, and optimization algorithms. The grid search technique systematically evaluates each combination within predefined ranges to determine the configuration that yields the best performance. This method has been widely utilized for hyperparameter optimization in machine learning tasks, as described in [41] and [42]. The process of grid search technique is as follows [45], [46].

1) *Select the hyperparameters to tune:*
   Identify the hyperparameters of your machine learning model that you want to optimize. These are typically parameters that are not learned from the data but need to be set before training
2) *Define the parameter grid:*
   Create a grid specifying the hyperparameter values to explore by defining a range of values or a list of possible values you want to test.
3) *Cross-validation setup and grid search iteration:*
   After setting up the cross-validation strategy, train and evaluate the ANN model using the chosen cross-validation strategy for each hyperparameters combination.
4) *Performance evaluation and select the best combination:*
   After each cross-validation iteration, the evaluation criteria are recorded, such as the loss value, against the current set of hyperparameters. Once all iterations are complete, select the one that yields the best results based on the interest performance metric.

This paper considers four types of hyperparameters: the number of neurons, the number of hidden layers, activation function, and optimization method. To generate a grid, the user-defined range of hyperparameters is as follows,
the number of neurons = [6 36 216]
hidden layers = [5 10 15 20]
activation = ['Relu' Tanh' 'Sigmoid']
optimizer = ['SGD' 'RMSprop' 'Adam']

E. DATA GENERATION AND TRAINING PROCESS

Fig. 4 shows the sensor geometry and true permittivity distribution for forward solver of ECT. In Fig. 4(a), it is the geometry and schematic layout of the electrical capacitance measurement sensor used in field study for obtaining capacitance data from the exhaust pipeline. The industrial pipe that carries the exhaust gases is made of steel and the pipe has an inner diameter of 35 mm and an outer diameter of 54.8 mm.

Number of electrodes used can influence the sensitivity and thus affect the quality of reconstructed images [47]. In this application since it involves metal pipe, electrodes are to be placed on the inner pipe boundary. Placing electrodes on inner boundary of steel pipe involves complex design and also additional cost of drilling. Thus, it is necessary to choose wisely the number of electrodes. In this application we have used an 8-electrode electrical capacitance measurement sensor featuring four electrodes in each plane with a width of 18mm aligning with inner surface of the pipe, is positioned along the exhaust pipeline.

Electrodes occupy more than 65% of the pipe circumference thus can have good sensitivity and satisfactory performance. Each electrode is equipped with a 20 mm-wide cap, and the space between the cap and the electrode is filled with Teflon, serving as an insulating material.

In generating simulated data, the finite element model is used to compute the capacitance values at the electrodes for given permittivity distribution of solid-gas flow. A fine mesh with 13713 triangular elements and 7067 nodes is used in numerical and industrial studies for free volume index estimation. The ECT forward solver generates capacitance values for training the artificial neural network model. These values account for residue deposit and gas flowing inside the pipe across various scenarios, each characterized by different volumes of gas and residue deposit. The exhaust gas residue accumulates on the inner walls of the pipe, while the gas flows through the pipe's center. Fig. 4(b) illustrates examples of cross-sectional true permittivity distributions used to generate capacitance values for the training process in the numerical simulation. Also, in order to consider effect of temperature in the semiconductor process, the permittivity value of the deposit was randomly varied by around 10% when calculating capacitance value. The dataset comprises a total of 3000 true permittivity distributions, spanning gas volumes from 0% to 100% at randomized positions within the pipe. Capacitance values for each distribution are computed using the ECT forward solver.

Fig. 5 illustrates the training procedure, encompassing data generation, segmentation of capacitance dataset into training and validation sets, and hyperparameter optimization using grid search techniques on the training dataset. The capacitance dataset, generated initially, is divided into two subsets: one for training the ANN and the other for validating the trained network. This process involves random shuffling of dataset, resulting in 2500 sets for training data and 500 sets for performance evaluation. Subsequently, grid search techniques are applied to identify optimal hyperparameters within the training dataset.

To determine the optimal hyperparameter combination, neural network models with each hyperparameter combination from the grid are trained for 200 epochs, and the best combination is selected based on the minimum loss value observed at the end.

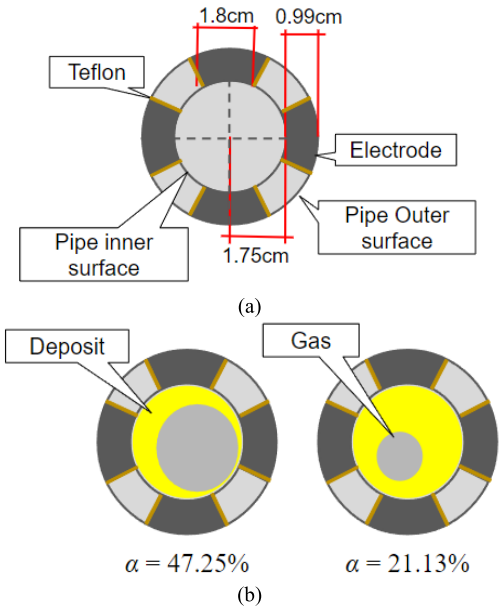

FIGURE 4. ECT sensor used in the studies and permittivity distribution for residue deposition monitoring, (a) ECT sensor geometry, (b) true permittivity distribution at $\alpha = 47.25\%$ and $\alpha = 21.13\%$.

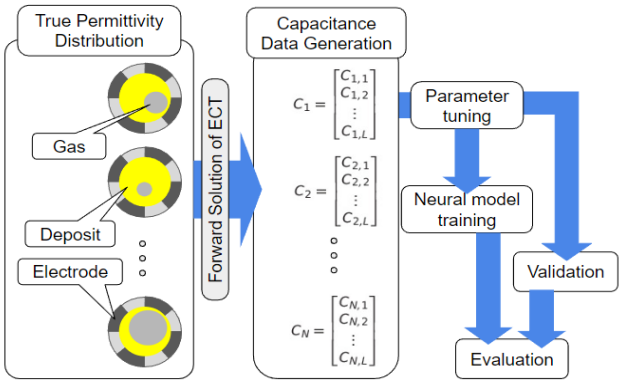

FIGURE 5. Training process for the proposed neural network model.

In the hyperparameter tuning process, the optimal parameters chosen for the ANN used in both the numerical and experimental studies include 35 neurons, 15 hidden layers, tanh activation function, and RMSprop optimizer. The computation of ANN networks for both numerical and experimental data is performed using a desktop computer equipped with an Intel(R) Core(TM) i7-6700 CPU @ 3.40GHz processor and 8 GB of RAM.

F. TUNNING RESULTS OF ANN

In order to confirm the performance of ANN model with optimal parameters, ANN models are trained with three hyperparameter combinations. First model consists of the optimal parameter chosen by grid search technique. Second model consists of 36 neurons, 15 hidden layers, Relu activation function and Adam optimizer. Third model consists of 36 neurons, 15 hidden layers, sigmoid activation function

and SGD optimizer. Three ANN models are trained for 1000 epochs using same training data, respectively.

Figure 6 depicts the variation in training loss throughout the training process for the three models. The graph reveals that the first model, selected using the grid search technique, achieves the fastest convergence below epoch 100. Furthermore, it is evident that while the models using Adam and SGD optimizers show a reduction in loss during training, their loss values exhibit instability.

Process of decreasing the training loss value. For both models, the loss value did not converge during the end of training.

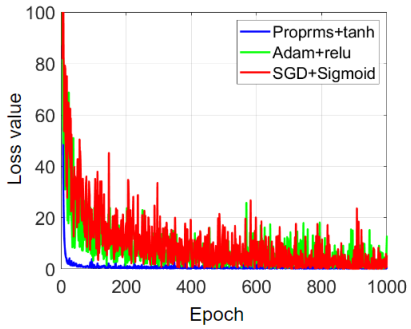

FIGURE 6. Loss value for void fraction estimation with hyperparameters selected by grid search technique in the training process.

G. PERFORMANCE METRICS FOR ANN

For performance evaluation and evaluating ANN accuracy, we have considered statistical parameters such as, coefficient of determination R^2, mean square percentage error (MSPE), mean absolute error (MAE), and root mean square error (RMSE), which are defined below.

The coefficient R^2 serves as an indicator of the accuracy of data fitting and is defined as

$$R^2 = 1 - \frac{\sum_{i=1}^{N} (\alpha_i^{true} - \alpha_i^{est})^2}{\sum_{i=1}^{N} (\alpha_i^{true} - \bar{\alpha^{est}})^2} \tag{19}$$

where $\alpha_i^{true}, \alpha_i^{est}$ are the true and estimated free volume indexes, $\bar{\alpha^{est}}$ is the mean of all estimated free volume index values. The parameter R^2 has maximum value as unity, and a greater value signifies a strong agreement between the estimated and true free volume index.

MSPE quantifies the expected squared distance between the prediction made by the predictor for a particular value and the actual true value, i.e.,

$$\text{MSPE} = \frac{100\%}{N} \sum_{i=1}^{N} \left(\frac{\alpha_i^{true} - \alpha_i^{est}}{\alpha_i^{true}}\right)^2 \tag{20}$$

MAE, a statistical parameter, quantifies the average absolute errors between true and predicted values. Smaller MAE values indicate higher accuracy of the prediction model. MAE is expressed as

$$\text{MAE} = \frac{1}{N} \sum_{i=1}^{N} \left|\alpha_i^{true} - \alpha_i^{est}\right| \tag{21}$$

RMSE serves as a performance metric indicating the accuracy of the ANN model. It is calculated as the square root of the mean squared error between the true and estimated free volume indexes, and is expressed as

$$\text{RMSE} = \frac{1}{N} \sum_{i=1}^{N} \frac{\left|\alpha_i^{true} - \alpha_i^{est}\right|}{\left|\alpha_i^{true}\right|} \times 100 \tag{22}$$

The RMSE value varies from 0 to 100%, and lower the value, the less the error is between predicted and actual value.

IV. EXPERIMENTAL SETUP

A. SEMICONDUCTOR PROCESS INDUSTRIAL SETUP

The dry etching and chemical vapor deposition (CVD) processes are essential in semiconductor device manufacturing. These processes involve a wafer processing system consisting of a process chamber where selected gases and chemicals are introduced through a feeder, depositing a thin layer over the substrate. The gases are managed by a gas control panel, which regulates their flow into the process chamber. During the process, the gases not only coat the substrate but also interact with the chamber walls and internal surfaces. Reaction byproducts and unreacted gases exit the chamber through a throttle valve and are pumped out via a vacuum system connected to a scrubber, which treats the residues before discharge.

To maintain process efficiency, the temperature inside the chamber is kept above 200°C. Gases exiting through **exhaust** pipelines may still contain reactive compounds, and residues, ranging from 100 nm to several microns in size, gradually accumulate inside the pipes, leading to clogging. Additionally, the scrubber's exhaust pipeline incorporates a high-temperature burn-off method to neutralize harmful gases. However, residue accumulation increases at lower temperatures, making it necessary to maintain temperatures above 200°C to prevent excessive buildup.

An electrical capacitance tomography (ECT) sensor was installed between the vacuum pump exit and the scrubber to monitor the deposition process and understand residue buildup. Figure 7 illustrates the schematic layout of the industrial setup for pipe deposition monitoring using ECT, while Table 1 lists the gases used in the process chamber.

TABLE 1. List of gases and byproducts formed in semiconductor process.

Process	Gas
Chemical vapor deposition	SiH4, B2H6, PH3, WF6, SiH2Cl2
Dry etch	He, NF3, BCL3, Cl2

V. RESULTS AND DISCUSSION

A. SIMULATION RESULTS

In numerical simulations, each scenario is initially designed with a homogeneous flow distribution within the exhaust pipe, primarily consisting of gas. Over time, powder-like residue accumulates and adheres to the inner wall of the pipe.

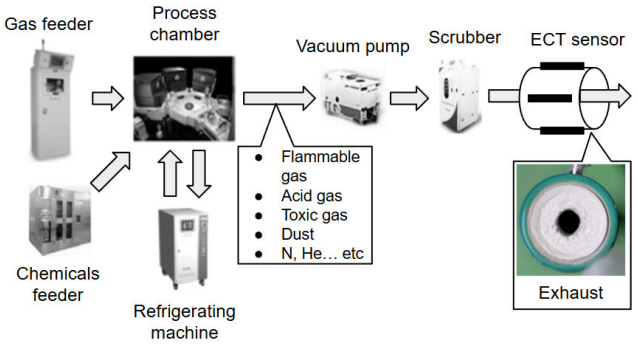

FIGURE 7. Schematic view of components and processes in the industrial setup for residue deposition monitoring in exhaust gas pipeline of semiconductor device manufacturing.

As time progresses, the thickness of the residue deposit increases, restricting the gas flow to the center portion of the pipe. To compare the performance of proposed three ANN-based models for free volume index estimation, three different scenarios are considered, each featuring annular and eccentric flow configurations.

In Scenario 1, the focus is on annular flow conditions, where gas flows concentrically in the center of the pipe while residue deposits accumulate along the inner wall. Eight test cases representing different stages of gas-residue deposition were examined for free volume index estimation using three distinct ANN models. The initial free volume index starts at 90.3% for test case 1 and progressively decreases, reaching 18.5% by the final test case 8. Figure 8(a) presents the true free volume index with gas-residue distribution across all eight test cases, while Figure 8(b) shows the estimated results from the three ANN models. The black curve represents the true free volume index, and the blue, green, and red curves represent the predictions from ANN models 1, 2, and 3, respectively.

It is observed that ANN model 1, which utilizes Tanh as the activation function and RMSPROP as the optimization method, provides the most accurate free volume index estimations across all test cases compared to ANN model 2 (ReLU + ADAM) and ANN model 3 (Sigmoid + SGD). When the free volume index exceeds 30%, ANN models 2 and 3 exhibit higher estimation errors. Specifically, ANN model 2 consistently underestimates the free volume index, while ANN model 3 tends to overestimate it.

The performance metrics R^2, RMSE, MSPE, and MAE for Scenario 1 are summarized in Table 2. ANN model 1 achieves an R^2 value of 0.99, indicating near-perfect accuracy, with the lowest MAE (0.89), MSPE (0.05), and RMSE (1.88) among the three models. Although ANN model 2 also has a high R^2 value of 0.99, its error metrics—MAE (1.30), MSPE (1.80), and RMSE (3.39)—are higher than those of model 1 but better than model 3. ANN model 3, as depicted in Figure 8(b), consistently underestimates the free volume index, resulting in significantly higher MAE, MSPE, and RMSE values.

Scenario 2 examines a more practical situation where the gas flow is slightly offset from the center of the exhaust pipe.

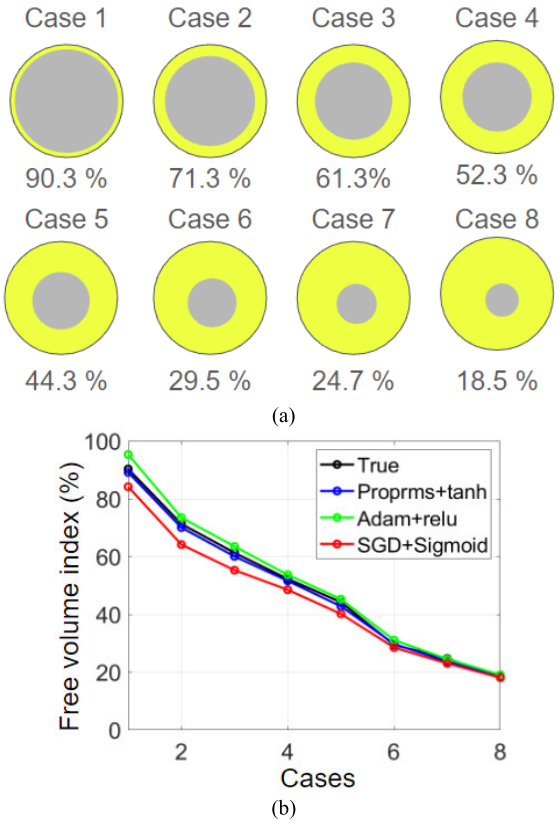

FIGURE 8. Simulation results for free volume index estimation in scenario 1 involving annular flow conditions with eight test cases. (a) true permittivity distribution and free volume index (b) estimation results for free volume index using ANN models.

Eight test cases (cases 9–16) were analyzed for free volume index estimation in this scenario, as shown in Figure 9. Figure 9(a) presents the true permittivity distribution corresponding to free volume indices ranging from 78.9% to 6.7%. In Figure 9(b), the black curve represents the true free volume index, while the blue, green, and red curves depict the estimated values from the 1st, 2nd, and 3rd ANN models, respectively.

It is clear from Figure 9(b) that the 1st model consistently provides the most accurate estimates across all eccentric test cases. While the 2nd and 3rd models demonstrate reasonable performance when the free volume index is below 20%, their accuracy declines significantly when the free volume index exceeds 20%, especially in comparison to the 1st model.

In Scenario 2, the 1st ANN model shows strong performance metrics, achieving an R^2 value of 0.99, with the lowest MAE (0.64), MSPE (0.11), and RMSE (2.51) among the three models. Although there is a slight increase in the error metrics compared to Scenario 1 (concentric flow), the 1st model remains highly effective in estimating free volume index even in more challenging eccentric flow conditions.

In Scenario 3, the test data represent a more complex situation where gas flow occurs at random locations inside the pipe, with residue deposits attached to the walls. Eight test cases (cases 17–24) were analyzed for free volume

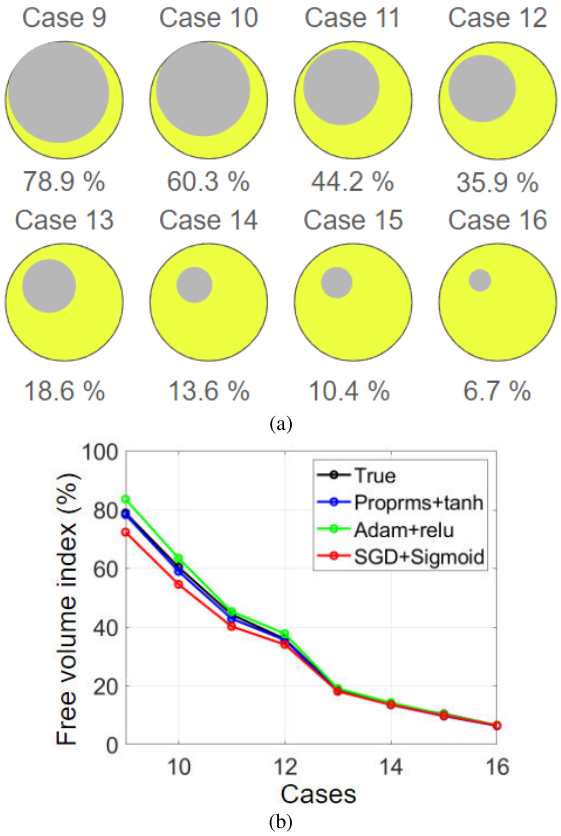

FIGURE 9. Simulation results for free volume index estimation in scenario 2 considering residue deposit and gas distribution within pipe (a) true permittivity distribution and free volume index, (b) estimation results for free volume index using ANN models.

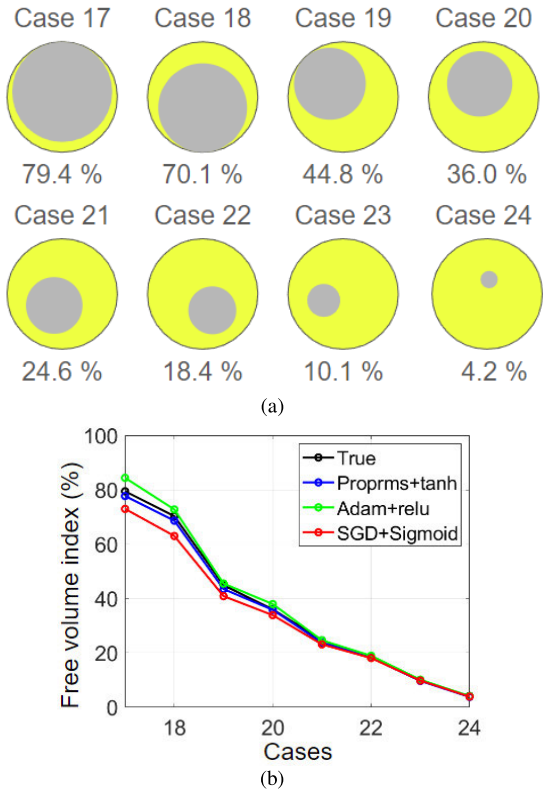

FIGURE 10. Simulation results for free volume index estimation in scenario 3, considering residue deposit and gas distribution within an exhaust pipe. (a) true permittivity distribution and free volume index (b) estimation results for free volume index using ANN models.

index estimation. Figure 10(a) illustrates the true permittivity images for free volume indices ranging from 79.4% to 4.2%, showing the gas and residue distribution within the pipe.

Figure 10(b) presents the free volume index estimation results for Scenario 3 using the three ANN models. The 1st model accurately estimated the free volume index across all test cases, while the 2nd and 3rd models exhibited estimation errors when the free volume index exceeded 40%. Consistent with the observations from Scenarios 1 and 2, the 2nd model overestimated the free volume index, whereas the 3rd model tended to underestimate it.

Performance metrics for Scenario 3 are shown in Table 2. The 1st model achieved the best results, with an R^2 value of 0.99, and lower MSPE (0.11), MAE (0.87), and RMSE (3.44) compared to the other two models. Notably, the 2nd model performed better in Scenario 3 than in Scenario 2, while the 3rd model showed higher error values, confirming that the 1st model remains the most reliable across all scenarios.

TABLE 2. Performance metric of ANN for free volume index estimation.

Metrics	ANN Model	Numerical studies			Experimental data
		Sc 1	Sc 2	Sc 3	
R^2	1st	0.99	0.99	0.99	-
	2nd	0.99	0.99	0.99	-
	3rd	0.96	0.97	0.97	-
MSPE	1st	0.05	0.11	0.11	3.84
	2nd	0.13	0.16	0.13	11.30
	3rd	0.55	0.40	0.47	4.25
MAE	1st	0.89	0.64	0.87	2.29
	2nd	1.80	1.51	1.33	3.93
	3rd	3.76	2.42	2.78	2.41
RMSE	1st	1.88	2.51	3.44	19.59
	2nd	3.39	3.66	3.30	33.62
	3rd	6.89	5.20	6.28	20.62

B. INDUSTRIAL FIELD STUDIES AND RESULTS

The electrical capacitance measurement sensor, detailed in Section IV-A, was installed along the exhaust pipeline of a semiconductor process at 'A' company. This sensor recorded independent capacitance values between the electrodes, enabling continuous monitoring of the pipeline conditions. The monitoring period spanned approximately three months, from June 1, 2020, to September 19, 2020. Capacitance data was collected at one-hour intervals, resulting in 2,100 data points over the course of the study, as shown in Fig. 11. During this period, the pipe remained mostly closed, providing a stable environment for validating both the initial and final conditions of the pipeline.

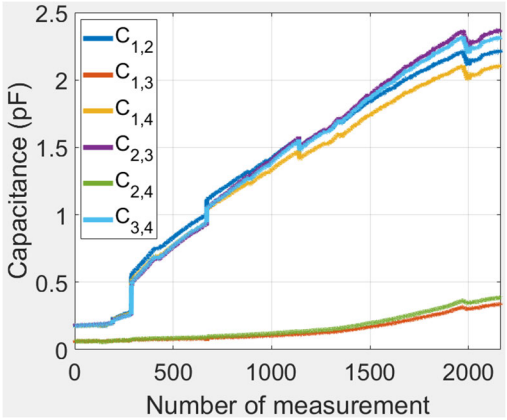

FIGURE 11. Measured capacitance data from the ECT sensor installed at the exhaust pipeline of the reaction chamber experimental facility of semiconductor company.

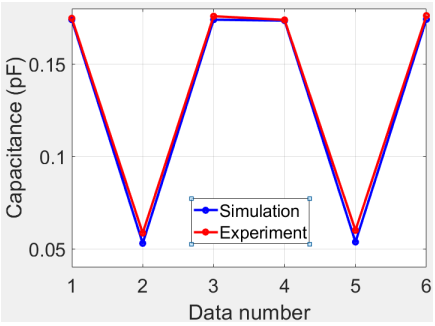

FIGURE 12. Capacitance values of numerical simulation and experiment at homogeneous case with only gas at cross sectional pipe.

Numerical simulations were conducted to calculate the capacitance under homogeneous gas conditions, and the results were compared with the initial measured capacitance data. As shown in Fig. 12, the comparison revealed a strong correlation between the simulated and actual measured data, confirming the accuracy and reliability of the capacitance measurements during the initial phase of the monitoring.

An ANN model, trained with simulated free volume index scenarios, was validated using 2,163 sets of capacitance measurements obtained from the field study. Analysis of the raw capacitance data (Fig. 11) shows an increase in the electrode pair capacitances over time. These capacitance readings were input into the ANN models to estimate the free volume index trend throughout the three-month monitoring period. As shown in Fig. 16, the initial estimated free volume index on June 1 at 9 AM was 95.9%, 96.2%, and 102.8% for the 1st, 2nd, and 3rd models, respectively, indicating a predominance of gaseous byproducts within the pipe. Up to case 289, the 1st model shows only a slight reduction in free volume index, while the 2nd and 3rd models show minimal or no change.

By case 460, the estimated free volume index from the 1st and 3rd models dropped to around 80%, reflecting the accumulation of residue particles along the inner walls of the pipeline. In contrast, the 2nd model's index only dropped to 90%, suggesting a smaller amount of

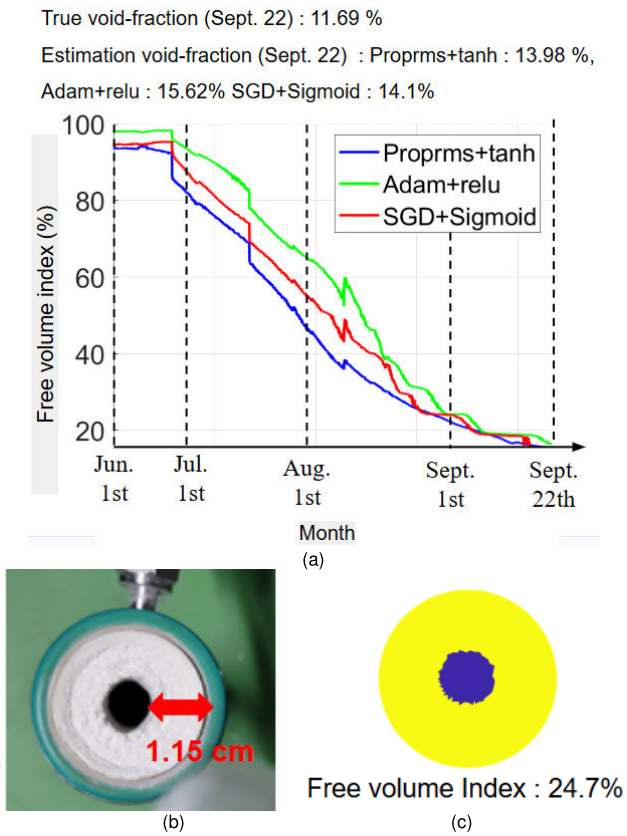

FIGURE 13. Experimental results for free volume index estimation through an exhaust pipeline of a reaction chamber in semiconductor process (a) free volume index estimation (b) true image of exhaust line pipe when the pipe is opened after the experiment for inspection, (c) Free volume index estimation using image based method.

residue accumulation. The free volume index continued to decrease rapidly thereafter, in line with the variations in capacitance data during the three-month measurement period (as shown in Fig. 13(a)). By September 1st, the free volume index estimates from all three models converged. However, until that point, the 1st model showed a steady decline in free volume index, while the 3rd model exhibited a more rapid drop beginning in August.

After the experiment, the pipeline was opened for inspection, revealing the residue deposition as illustrated in Figure 13(b). The thickness of the gas flow region was measured using inner Vernier calipers, yielding a true free volume index of 11.68%. On the final day of measurement, September 21, the estimated free volume index values from the 1st, 2nd, and 3rd models were 13.98%, 15.62%, and 14.1%, respectively. The estimated free volume index with ANN model 1 is close to the true measured value which shows great potentiality in using ANN model with capacitance measurements. The ANN models reported slight higher free volume index values and these discrepancies arise due to the models inability to fully account for variations in permittivity caused by temperature changes during the data generation process, despite incorporating a 10% adjustment for permittivity variations. Additionally, to compare

the performance of the proposed estimation method with image-based approaches, the inverse problem of Electrical Capacitance Tomography (ECT) was solved using Gauss Newton to reconstruct the permittivity distribution image. Using the Otsu method, the boundaries between gas and deposits were delineated, and the free volume fraction was calculated. Figure 13(c) shows a binarized image obtained by applying the Otsu method after image reconstruction. Based on this image, the calculated free volume fraction was 24.7%, which was significantly larger than the actual value.

The performance metrics for the experimental data are summarized in Table 2. During the measurement period, the exhaust pipeline remained closed, except for maintenance intervals, limiting the availability of true free volume index values. The final measurement provided the only true free volume index for comparison. Among the models, the 1st model outperformed the 2nd and 3rd models based on MSPE, MAE, and RMSE. For the 1st model, the MSPE, MAE, and RMSE were 2.29, 19.59, and 3.84, respectively, demonstrating superior performance. In contrast, the 2nd model exhibited lower accuracy, with MSPE, MAE, and RMSE values of 3.93, 33.62, and 11.30, respectively, for the final measurement. The 3rd model showed moderate improvement over the 2nd model, with MSPE, MAE, and RMSE values of 4.25, 2.41, and 20.62, respectively, but still underperformed compared to the 1st model.

VI. CONCLUSION

This study developed a monitoring system for residue deposition in industrial process exhaust pipelines using an electrical capacitance measurement sensor combined with an artificial neural network (ANN). The results demonstrate the efficacy of using capacitance measurements to estimate the free volume index, which is critical for understanding phase fractions of residue and gas in solid-gas flows. By training the ANN with capacitance data and permittivity distributions, the system achieved high precision in estimating the free volume index under both simulated and real-world conditions.

Among the three ANN models tested, the Tanh activation function with Proprms optimization yielded the most accurate results, particularly in scenarios with varying deposition levels. Field data collected over three months from a semiconductor fabrication facility validated the robustness of the system, with model predictions closely matching actual measurements. For example, on the final test day, the free volume index was measured at 11.69%, with ANN model 1 estimating it at 13.98%, showcasing the model's reliability. The estimated free volume index based on the traditional image based method was 24%.

Despite these successes, the study highlights several limitations and avenues for improvement. The ANN models assumed constant permittivity values for gas and residue, which may not hold true under real-world conditions due to temperature fluctuations and process variability. These factors can lead to inaccuracies in capacitance readings and subsequent free volume index estimations. Future work should address this limitation by incorporating variable permittivity values as dynamic inputs to the ANN, improving the model's adaptability to changing conditions.

In conclusion, the proposed system offers a practical, accurate, and scalable solution for real-time monitoring of residue deposition in semiconductor exhaust pipelines. This innovation enhances safety and operational efficiency by enabling proactive maintenance and hazard mitigation. Further research to refine the model and expand its applicability to dynamic process conditions will strengthen its utility in industrial environments.

ACKNOWLEDGMENT

The authors would like to thank the PROSEN team for providing experimental data from the semiconductor manufacturing company for testing.

REFERENCES

[1] G. S. May and C. J. Spanos, *Fundamentals of Semiconductor Manufacturing and Process Control*. Hoboken, NJ, USA: Wiley, 2006.

[2] M. F. Yoo, J. Wang, and J. C. Sheu, "Method for preventing clogging of reaction chamber exhaust lines," U.S. Patent 11 466 922, Feb. 28, 2008.

[3] K.-M. Choi, H.-C. An, and K.-S. Kim, "Identifying the hazard characteristics of powder byproducts generated from semiconductor fabrication processes," *J. Occupational Environ. Hygiene*, vol. 12, no. 2, pp. 114–122, Feb. 2015, doi: 10.1080/15459624.2014.955178.

[4] D.-W. Lee, S. Cho, and A. Shin, "Lymphohematopoietic cancer mortality among Korean semiconductor manufacturing workers," *BMC Public Health*, vol. 23, no. 1, p. 1473, Aug. 2023, doi: 10.1186/s12889-023-16325-z.

[5] M. Saeedi, B. Malekmohammadi, and S. Tajalli, "Interaction of benzene, toluene, ethylbenzene, and xylene with human's body: Insights into characteristics, sources and health risks," *J. Hazardous Mater. Adv.*, vol. 16, Nov. 2024, Art. no. 100459, doi: 10.1016/j.hazadv.2024.100459.

[6] D. Breitenmoser, A. Manera, H.-M. Prasser, R. Adams, and V. Petrov, "High-resolution high-speed void fraction measurements in helically coiled tubes using X-ray radiography," *Nucl. Eng. Design*, vol. 373, Mar. 2021, Art. no. 110888, doi: 10.1016/j.nucengdes.2020.110888.

[7] E. Nazemi, S. A. H. Feghhi, G. H. Roshani, R. G. Peyvandi, and S. Setayeshi, "Precise void fraction measurement in two-phase flows independent of the flow regime using gamma-ray attenuation," *Nucl. Eng. Technol.*, vol. 48, no. 1, pp. 64–71, Feb. 2016, doi: 10.1016/j.net.2015.09.005.

[8] M. Alamoudi, M. A. Sattari, M. Balubaid, E. Eftekhari-Zadeh, E. Nazemi, O. Taylan, and E. M. Kalmoun, "Application of gamma attenuation technique and artificial intelligence to detect scale thickness in pipelines in which two-phase flows with different flow regimes and void fractions exist," *Symmetry*, vol. 13, no. 7, p. 1198, Jul. 2021, doi: 10.3390/sym13071198.

[9] L. Fang, X. Yuan, Z. Zhang, C. Zhou, H. Li, M. Chen, and K. Lan, "An eight-channel-based near infrared void fraction measurement system using T-ART algorithm," *Opt. Lasers Eng.*, vol. 161, Feb. 2023, Art. no. 107385, doi: 10.1016/j.optlaseng.2022.107385.

[10] J. Huang, Y. Jiang, H. Ji, B. Wang, and Z. Huang, "Electrical impedance characteristics of slug flow in small channels and its application to void fraction estimation," *Int. J. Multiphase Flow*, vol. 156, Nov. 2022, Art. no. 104200, doi: 10.1016/j.ijmultiphaseflow.2022.104200.

[11] W. Q. Yang, M. S. Beck, and M. Byars, "Electrical capacitance tomography—From design to applications," *Meas. Control*, vol. 28, no. 9, pp. 261–266, Nov. 1995, doi: 10.1177/002029409502800901.

[12] M. V. Sardeshpande, S. Harinarayan, and V. V. Ranade, "Void fraction measurement using electrical capacitance tomography and high speed photography," *Chem. Eng. Res. Design*, vol. 94, pp. 1–11, Feb. 2015, doi: 10.1016/j.cherd.2014.11.013.

[13] H. Wang and W. Yang, "Application of electrical capacitance tomography in pharmaceutical fluidised beds—A review," *Chem. Eng. Sci.*, vol. 231, Feb. 2021, Art. no. 116236, doi: 10.1016/j.ces.2020.116236.

[14] U. Khan, W. Pao, N. Sallih, and F. Hassan, "Flow regime identification in gas-liquid two-phase flow in horizontal pipe by deep learning," *J. Adv. Res. Appl. Sci. Eng. Technol.*, vol. 27, no. 1, pp. 86–91, Jul. 2022, doi: 10.37934/araset.27.1.8691.

[15] A. Jaworek, A. Krupa, and M. Trela, "Capacitance sensor for void fraction measurement in water/steam flows," *Flow Meas. Instrum.*, vol. 15, nos. 5–6, pp. 317–324, Oct. 2004.

[16] J. A. Gutierrez, T. Dyakowski, F. J. Dickin, R. Thorn, R. C. Waterfall, R. A. Williams, C. G. Xie, and M. S. Beck, "Tomographic systems for measurement and control of minerals processing plants," *IFAC Proc. Vol.*, vol. 26, no. 2, pp. 535–538, Jul. 1993, doi: 10.1016/s1474-6670(17)48527-2.

[17] Y. D. Jiang and M. Soleimani, "Capacitively coupled electrical impedance tomography for brain imaging," *IEEE Trans. Med. Imag.*, vol. 38, no. 9, pp. 2104–2113, Sep. 2019, doi: 10.1109/TMI.2019.2895035.

[18] A. Voss, P. Hosseini, M. Pour-Ghaz, M. Vauhkonen, and A. Seppänen, "Three-dimensional electrical capacitance tomography—A tool for characterizing moisture transport properties of cement-based materials," *Mater. Design*, vol. 181, Nov. 2019, Art. no. 107967, doi: 10.1016/j.matdes.2019.107967.

[19] W. Li, W. Song, G. Yin, M. C. Ong, and F. Han, "Flow regime identification in the subsea jumper based on electrical capacitance tomography and convolution neural network," *Ocean Eng.*, vol. 266, Dec. 2022, Art. no. 113152, doi: 10.1016/j.oceaneng.2022.113152.

[20] Q. Guo, M. Ye, W. Yang, and Z. Liu, "A machine learning approach for electrical capacitance tomography measurement of gas–solid fluidized beds," *AIChE J.*, vol. 65, no. 6, Jun. 2019, Art. no. e16583, doi: 10.1002/aic.16583.

[21] G. T. Chala and B. M. Negash, "Artificial neural network and regression models for predicting intrusion of non-reacting gases into production pipelines," *Energies*, vol. 15, no. 5, p. 1725, Feb. 2022, doi: 10.3390/en15051725.

[22] H. Xie, H. Chen, X. Gao, X. Zheng, X. Zhi, and X. Zhang, "Theoretical analysis of fuzzy least squares support vector regression method for void fraction measurement of two-phase flow by multi-electrode capacitance sensor," *Cryogenics*, vol. 103, Oct. 2019, Art. no. 102969, doi: 10.1016/j.cryogenics.2019.07.008.

[23] A. Veisi, M. H. Shahsavari, G. H. Roshani, E. Eftekhari-Zadeh, and E. Nazemi, "Experimental study of void fraction measurement using a capacitance-based sensor and ANN in two-phase annular regimes for different fluids," *Axioms*, vol. 12, no. 1, pp. 66–78, Jan. 2023, doi: 10.3390/axioms12010066.

[24] X. Wang, Y. Chen, B. Wang, K. Tang, and H. Hu, "Sectional void fraction measurement of gas-water two-phase flow by using a capacitive array sensor," *Flow Meas. Instrum.*, vol. 74, Aug. 2020, Art. no. 101788, doi: 10.1016/j.flowmeasinst.2020.101788.

[25] D. He, S. Chen, and B. Bai, "Void fraction measurement of stratified gas-liquid flow based on multi-wire capacitance probe," *Experim. Thermal Fluid Sci.*, vol. 102, pp. 61–73, Apr. 2019, doi: 10.1016/j.expthermflusci.2018.11.005.

[26] J. Yao and M. Takei, "Application of process tomography to multi-phase flow measurement in industrial and biomedical fields: A review," *IEEE Sensors J.*, vol. 17, no. 24, pp. 8196–8205, Dec. 2017, doi: 10.1109/JSEN.2017.2682929.

[27] M. J. H. Khan, M. A. Hussain, Z. Mansourpour, N. Mostoufi, N. M. Ghasem, and E. C. Abdullah, "CFD simulation of fluidized bed reactors for polyolefin production—A review," *J. Ind. Eng. Chem.*, vol. 20, no. 6, pp. 3919–3946, Nov. 2014, doi: 10.1016/j.jiec.2014.01.044.

[28] J. Lei, H. P. Mu, Q. B. Liu, X. Y. Wang, and S. Liu, "Data-driven reconstruction method for electrical capacitance tomography," *Neurocomputing*, vol. 273, pp. 333–345, Jan. 2018, doi: 10.1016/j.neucom.2017.08.006.

[29] A. Mezouar, N. Saidi-Amroun, V. Griseri, G. Teyssedre, and M. Saidi, "Correlation between chemical, thermal and dielectric properties of gamma-irradiated PTFE thin films," *J. Polym. Res.*, vol. 30, no. 2, p. 88, Jan. 2023.

[30] U. Rosenbaum, J. A. Huisman, J. Vrba, H. Vereecken, and H. R. Bogena, "Correlation of temperature and electrical conductivity effects on dielectric permittivity measurement with ECH_2O senser," *Vadose Zone J.*, vol. 10, no. 2, pp. 582–593, May 2011.

[31] M. Kim, K. Komeda, J. Jeong, M. Oinuma, T. Sato, and K. Saito, "Optimizing calibration for a capacitance-based void fraction sensor with asymmetric electrodes under horizontal flow in a smoothed circular macrotube," *Sensors*, vol. 22, no. 9, p. 3511, May 2022, doi: 10.3390/s22093511.

[32] A. M. Iliyasu, F. Fouladinia, A. S. Salama, G. H. Roshani, and K. Hirota, "Intelligent measurement of void fractions in homogeneous regime of two phase flows independent of the liquid phase density changes," *Fractal Fractional*, vol. 7, no. 2, p. 179, Feb. 2023, doi: 10.3390/fractalfract7020179.

[33] Z. Kan, X. Liu, and S. Jia, "Void fraction measurement of gas-liquid two-phase flow based on capacitance sensor," *IEEE Trans. Instrum. Meas.*, vol. 73, pp. 1–10, 2024, doi: 10.1109/TIM.2024.3472773.

[34] M. A. Al-Fayoumi, H. M. Al-Mimi, A. Veisi, H. Al-Aqrabi, M. S. Daoud, and E. Eftekhari-Zadeh, "Utilizing artificial neural networks and combined capacitance-based sensors to predict void fraction in two-phase annular fluids regardless of liquid phase type," *IEEE Access*, vol. 11, pp. 143745–143756, 2023, doi: 10.1109/ACCESS.2023.3340127.

[35] T.-C. Chen, S. M. Alizadeh, A. K. Alanazi, J. W. G. Guerrero, H. M. Abo-Dief, E. Eftekhari-Zadeh, and F. Fouladinia, "Using ANN and combined capacitive sensors to predict the void fraction for a two-phase homogeneous fluid independent of the liquid phase type," *Processes*, vol. 11, no. 3, p. 940, Mar. 2023, doi: 10.3390/pr11030940.

[36] C. Tan, S. Lv, F. Dong, and M. Takei, "Image reconstruction based on convolutional neural network for electrical resistance tomography," *IEEE Sensors J.*, vol. 19, no. 1, pp. 196–204, Jan. 2019, doi: 10.1109/JSEN.2018.2876411.

[37] W. Q. Yang and L. Peng, "Image reconstruction algorithms for electrical capacitance tomography," *Meas. Sci. Technol.*, vol. 14, no. 1, pp. R1–R13, Dec. 2002, doi: 10.1088/0957-0233/14/1/201.

[38] D. Svozil, V. Kvasnicka, and J. Pospichal, "Introduction to multi-layer feed-forward neural networks," *Chemometric Intell. Lab. Syst.*, vol. 39, no. 1, pp. 43–62, Nov. 1997, doi: 10.1016/s0169-7439(97)00061-0.

[39] S. Abid, F. Fnaiech, and M. Najim, "A fast feedforward training algorithm using a modified form of the standard backpropagation algorithm," *IEEE Trans. Neural Netw.*, vol. 12, no. 2, pp. 424–430, Mar. 2001, doi: 10.1109/72.914537.

[40] S. Sharma, S. Sharma, and A. Athaiya, "Activation functions in neural networks," *Int. J. Eng. Appl. Sci. Technol.*, vol. 4, no. 12, pp. 310–316, May 2020, doi: 10.33564/ijeast.2020.v04i12.054.

[41] Q. Song, J. Xiao, and Y. C. Soh, "Robust backpropagation training algorithm for multilayered neural tracking controller," *IEEE Trans. Neural Netw.*, vol. 10, no. 5, pp. 1133–1141, Sep. 1999, doi: 10.1109/72.788652.

[42] N. Landro, I. Gallo, and R. La Grassa, "Mixing Adam and SGD: A combined optimization method," 2020, *arXiv:2011.08042*.

[43] V. Deshwal and M. Sharma, "Breast cancer detection using SVM classifier with grid search technique," *Int. J. Comput. Appl.*, vol. 178, no. 31, pp. 18–23, Jul. 2019.

[44] M. Edalatifar, M. B. Tavakoli, M. Ghalambaz, and F. Setoudeh, "Using deep learning to learn physics of conduction heat transfer," *J. Thermal Anal. Calorimetry*, vol. 146, no. 3, pp. 1435–1452, Jul. 2020, doi: 10.1007/s10973-020-09875-6.

[45] H. Chen, Z. Liu, K. Cai, L. Xu, and A. Chen, "Grid search parametric optimization for FT-NIR quantitative analysis of solid soluble content in strawberry samples," *Vibrational Spectrosc.*, vol. 94, pp. 7–15, Jan. 2018, doi: 10.1016/j.vibspec.2017.10.006.

[46] Q. Wang, W. Zheng, F. Wu, H. Zhu, A. Xu, Y. Shen, and Y. Zhao, "Improving the SSH retrieval precision of spaceborne GNSS-R based on a new grid search multihidden layer neural network feature optimization method," *Remote Sens.*, vol. 14, no. 13, pp. 3161–3179, Jul. 2022, doi: 10.3390/rs14133161.

[47] L. Peng, J. Ye, G. Lu, and W. Yang, "Evaluation of effect of number of electrodes in ECT sensors on image quality," *IEEE Sensors J.*, vol. 12, no. 5, pp. 1554–1565, May 2012, doi: 10.1109/JSEN.2011.2174438.

MINHO JEON was born in Jeju, South Korea, in 1989. He received the B.Eng. degree in electronic engineering from Jeju National University, Jeju, in 2014, and the M.Sc. degree in electronic engineering from the Faculty of Applied Energy System, Jeju National University, in 2016, where he is currently pursuing the Ph.D. degree. His research interests include electrical impedance tomography, deep learning, machine learning, and estimation theory.

ANIL KUMAR KHAMBAMPATI received the B.S. degree in mechanical engineering from Jawaharlal Nehru Technological University, India, in 2003, and the M.S. degree in marine instrumentation engineering and the Ph.D. degree in electronic engineering from Jeju National University, South Korea, in 2006 and 2010, respectively. He is currently a Research Professor with the Department of Electronic Engineering, Jeju National University. His research interests include electrical impedance tomography, electrical capacitance tomography, inverse problems, and optimal control.

JONG HYUN SONG received the B.S. degree in chemical engineering from Chung-Ang University, Seoul, South Korea, in 2017, and the M.S. degree in electronics engineering from Chungnam National University, Daejeon, South Korea, in 2023, where he is currently pursuing the Ph.D. degree.

From 2017 to 2019, he worked for LG Display pOLED Division in Paju. He is a Senior Researcher with the KAIST Affiliated National Nano Fab Center for Diffusion Process, Daejeon. His research interests include the development of diffusion technology, ECT sensor, and monolithic 3D integration.

KEUN JOONG YOON received the B.E. degree in computer engineering from Kwangwoon University, South Korea, in 1988, and the M.Sc. degree in computer engineering from Kwangwoon University, in 1990. He has worked in S/W application and sensor design related to electronic capacitance sensing. He is currently with Prosen Company Ltd. which works on modeling and development of tomography measurement device, 2D laser sensing device, and confocal sensing device.

KYUNG YOUN KIM received the B.S., M.S., and Ph.D. degrees in electronic engineering from Kyungpook National University, Daegu, South Korea, in 1983, 1986, and 1990, respectively. From 1994 to 1995, he was a Postdoctoral Fellow with the Department of Electrical Engineering, University of Maryland at Baltimore County (UMBC), Baltimore, MD, USA. From 2001 to 2002, he was a Visiting Professor with the Department of Applied Physics, Kuopio University, Kuopio, Finland. Since 1990, he has been with the Department of Electronic Engineering, Jeju National University, Jeju, South Korea, where he is currently a Professor. Since 2004, he has been a Visiting Professor with the Department of Biomedical Engineering, Rensselaer Polytechnic Institute (RPI), Troy, NY, USA. His current research interests include estimation theory, inverse problems, intelligent fault detection and diagnosis, instrumentation and control, and electrical impedance tomography.